The International Journal of Advanced Manufacturing Technology
https://doi.org/10.1007/s00170-022-10669-3

ORIGINAL ARTICLE

Fatigue strength analysis of bimetallic sleeve roll by simulation of local slip accumulation at shrink-fit interface caused by roll rotation

Nao-Aki Noda[1] · Rahimah Abdul Rafar[1] · Xuchen Zheng[1] · Hiroyuki Tsurumaru[1] · Yudai Taruya[1] · Yoshikazu Sano[1] · Yasushi Takase[1]

Received: 15 May 2022 / Accepted: 6 December 2022

Abstract
Next generation rolls such as super-cermet rolls and all-ceramic rolls can be only manufactured as sleeve rolls, although the circumferential slippage appears at the shrink-fit interface. In this study, the fatigue strength of the sleeve roll is evaluated by applying the load shifting method on the fixed roll to realize the local slip accumulation during roll rotation. The simulation shows that the fatigue-inducing stress amplitude remains constant although the accumulated slip amount increases. Based on those results, the fatigue strength of standard rolling rolls is estimated considering the slip defect. The defect dimension can be characterized by the root area parameter and the value $\sqrt{\text{area}}$ =1254 μm can be estimated from smaller roll experimental results and the previous report for larger diameter sleeve rolls. The results show that in the absence of slip damage, the fatigue strength of sleeve rolls is not much lower than that of solid rolls without shrink-fit.

Keywords Sleeve roll · Shrink-fitting · Bimetallic work roll · Local slip accumulation · Load shifting method · Fatigue strength evaluation · Residual stress

Nomenclature

B_0^{270}	Critical point on HSS/DCI boundary where $(r, z) = (270\text{mm}, 0)$
B_{750}^{270}	Critical point on HSS/DCI boundary where $(r, z) = (270\text{mm}, 750\text{mm})$
b'	Defect depth of the sleeve roll with body diameter $D = 1150$ mm (mm)
C_0^0	Critical point at center point where $(r, z) = (0, 0)$
D	Outer diameter of the sleeve (mm)
DCI	Ductile casting iron
d	Inner diameter of sleeve in Fig. 1A (mm)
d_1	Inner diameter of sleeve 1 in Fig. 1B (mm)
d_2	Inner diameter of sleeve 2 in Fig. 1B (mm)
E	Rolling stress $\sigma_\theta^{\text{Rolling}}$ (MPa)
E_{sleeve}	Young's modulus of sleeve (GPa)
E_{shaft}	Young's modulus of shaft (GPa)
F	Sum of $\sigma_\theta^{\text{Res+Shrink}} + \sigma_\theta^{\text{Rolling}}$ (MPa)
FEM	Finite element method
HSS	High-speed steel
H_V	Vickers hardness (kgf/mm^2)
P	Load from back-up roll and hot strip (N)
P_0	Concentrated load per unit width = standard compressive force (N/mm)
P_b	Bending force from bearing per unit width (N/mm)
P_b^*	Bending force from bearing (N)
P_h	Rolling reaction force (N)
R	Stress ratio is defined as the ratio of minimum stress to maximum stress
r	Radius (mm)
S	Frictional force from the rolling plate (N)
T	Driving torque (Nm)
T_m	Motor torque per unit width = Standard drive torque (Nm/mm)
T_m^*	Rated torque of motor (Nm)
T_r	Resistance torque per unit width = 3193 Nm/mm

✉ Nao-Aki Noda
noda.naoaki844@mail.kyutech.jp

[1] Mechanical Engineering Department, Kyushu Institute of Technology, 1-1 Sensui-Cho, Tobata-Ku, Kitakyushu-Shi 804-8550, Japan

Published online: 26 December 2022

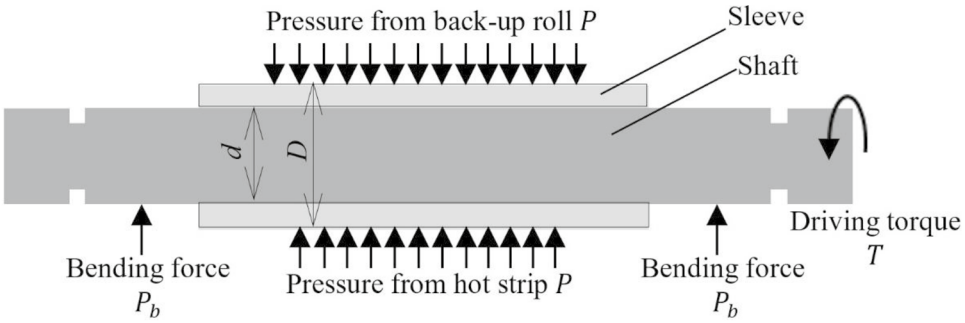

(A) Single material sleeve roll.

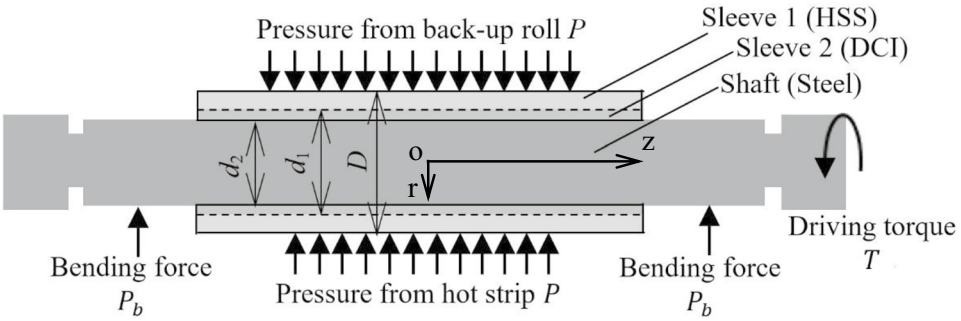

(B) Bimetallic sleeve roll with D=700 mm, d_1=540 mm, d_2= 450 mm.

Fig. 1 Schematic illustration for the standard roll used in real hot strip rolling

T_r^*	Slippage resistance torque (Nm)
$u_\theta(\theta)$	Interfacial displacement (mm)
u_θ^{sleeve}	Circumferential displacement of the sleeve (mm)
u_θ^{shaft}	Circumferential displacement of the shaft (mm)
$u_\theta^{P(0)\sim P(\varphi)}(\theta)$	Interfacial slip u_θ when the pair of loads $P = P_0$ are applied at $\varphi = 0$ $(\varphi = \pi)$ to $\varphi = \varphi\,(\varphi = \varphi + \pi)$ (mm)
$u_{\theta,sleeve}^{P(0)\sim P(\varphi)}(\theta)$	Interfacial slip u_θ when the pair of loads $P = P_0$ are applied at the inner surface of the sleeve at $\varphi = 0\,(\varphi = \pi)$ to $\varphi = \varphi\,(\varphi = \varphi + \pi)$ (mm)
$u_{\theta,shaft}^{P(0)\sim P(\varphi)}(\theta)$	Interfacial slip u_θ when the pair of loads $P = P_0$ are applied at the outer surface of the shaft at $\varphi = 0\,(\varphi = \pi)$ to $\varphi = \varphi\,(\varphi = \varphi + \pi)$ (mm)
$u_{\theta,ave.}^{P(0)\sim P(\varphi)}$	Average displacement due to the pair of loads shifting from $\varphi = 0\,(\varphi = \pi)$ to $\varphi = \varphi\,(\varphi = \varphi + \pi)$ (mm)
$u_{\theta,T=T_m}^{P(0)\sim P(\varphi)}(\theta)$	Interfacial slip u_θ under standard drive torque $T = T_m$ when the pair of loads $P = P_0$ are applied at $\varphi = 0\,(\varphi = \pi)$ to $\varphi = \varphi\,(\varphi = \varphi + \pi)$ (mm)
$u_{\theta,T=T_m}^{P(0)}(\theta)$	Interfacial slip u_θ under standard drive torque $T = T_m$ when the pair of loads $P = P_0$ are applied at $\varphi = 0\,(\varphi = \pi)$ (mm)
$u_{\theta,T=T_m}^{P(0)\sim P(2\varphi)}(\theta)$	Interfacial slip u_θ under standard drive torque $T = T_m$ when the pair of loads $P = P_0$ moves one rotation at $\varphi = 0$ $(\varphi = \pi)$ to $\varphi = 2\varphi\,(\varphi = \varphi + \pi)$ (mm)
$u_{\theta,T=T_m}^{P(0)\sim P(4\varphi)}(\theta)$	Interfacial slip u_θ under standard drive torque $T = T_m$ when the pair of loads $P = P_0$ move two rotations at $\varphi = 0$ $(\varphi = \pi)$ to $\varphi = 4\varphi\,(\varphi = \varphi + \pi)$ (mm)
$u_{\theta,ave.T=T_m}^{P(0)\sim P(\varphi)}$	Average displacement under standard drive torque $T = T_m$ due to the pair of loads $P = P_0$ shifting from $\varphi = 0$ $(\varphi = \pi)$ to $\varphi = \varphi\,(\varphi = \varphi + \pi)$ (mm)
δ	Tightening allowance between sleeve inner diameter and shaft outer diameter (mm)
θ	Circumferential displacement angle (°)
μ	Friction coefficient between sleeve and shaft

υ_{sleeve} Poisson's ratio of sleeve
υ_{shaft} Poisson's ratio of shaft
σ_{a} Stress amplitude (MPa)
σ_B Ultimate tensile strength (MPa)
σ_{m} Mean stress (MPa)
σ_{r} Contact stress at the inner surface of the sleeve (MPa)
$\sigma_{r,\mathrm{shrink}}$ Contact stress during shrink-fitting (MPa)
$\sigma_{r,T=T_m}^{P(0)\sim P(\varphi)}(\theta)$ Contact stress σ_r under standard drive torque $T = T_m$ due to the load shifting $P(0) \sim P(\varphi)$ from the angle $\varphi = 0$ $(\varphi = \pi)$ to $\varphi = \varphi\,(\varphi = \varphi + \pi)$ (MPa)
$\sigma_r^{P(0)\sim P(4\pi)}(\theta)$ Contact stress σ_r due to the load $P = P_0$ moves two rotations (MPa)
$\sigma_{r,T=T_m}^{P(0)\sim P(4\pi)}(\theta)$ Contact stress σ_r under standard drive torque $T = T_m$ due to the load $P = P_0$ moves two rotations (MPa)
$\sigma_{r,T=1.1T_m}^{1.1P(0)\sim 1.1P(4\pi)}(\theta)$ Contact stress σ_r under standard drive torque $T = 1.1T_m$ due to the load $P = 1.1P_0$ moves two rotations (MPa)
$\sigma_{r,T=1.2T_m}^{1.2P(0)\sim 1.2P(4\pi)}(\theta)$ Contact stress σ_r under standard drive torque $T = 1.2T_m$ due to the load $P = 1.2P_0$ moves two rotations (MPa)
$\sigma_{r,T=1.3T_m}^{1.3P(0)\sim 1.3P(4\pi)}(\theta)$ Contact stress σ_r under standard drive torque $T = 1.3T_m$ due to the load $P = 1.3P_0$ moves two rotations (MPa)
$\sigma_{r,T=1.4T_m}^{1.4P(0)\sim 1.4P(4\pi)}(\theta)$ Contact stress σ_r under standard drive torque $T = 1.4T_m$ due to the load $P = 1.4P_0$ moves two rotations (MPa)
$\sigma_{r,T=1.5T_m}^{1.5P(0)\sim 1.5P(4\pi)}(\theta)$ Contact stress σ_r under impact force $T = 1.5T_m$ due to the load $P = 1.5P_0$ moves two rotations (MPa)
σ_θ Rolling stress at the inner surface of the sleeve (MPa)
$\sigma_{\theta\max}$ Maximum stress (MPa)
$\sigma_{\theta\min}$ Minimum stress (MPa)
$\sigma_{\theta,\mathrm{shrink}}$ Interface stress during shrink-fitting (MPa)
$\sigma_{\theta\max}^{P_0}$ Maximum stress under the load $\mathrm{P} = P_0$ (MPa)
$\sigma_{\theta\min}^{P_0}$ Minimum stress under the load $\mathrm{P} = P_0$ (MPa)
$\sigma_{\theta\max}^{1.5P_0}$ Maximum stress under the load $\mathrm{P} = 1.5P_0$ (MPa)
$\sigma_{\theta\min}^{1.5P_0}$ Minimum stress under the load $\mathrm{P} = 1.5P_0$ (MPa)
$\sigma_\theta^{P(0)\sim P(\varphi)}(\theta)$ Interface stress σ_θ due to the load shifting $P(0) \sim P(\varphi)$ from the angle $\varphi = 0\,(\varphi = \pi)$ to $\varphi = \varphi\,(\varphi = \varphi + \pi)$ (MPa)
$\sigma_{\theta,T=T_m}^{P(0)\sim P(2\varphi)}(\theta)$ Interface stress σ_θ under standard drive torque $T = T_m$ due to the load $P = P_0$ moves one rotation (MPa)
$\sigma_{\theta,T=T_m}^{P(0)\sim P(4\varphi)}(\theta)$ Interface stress σ_θ under standard drive torque $T = T_m$ due to the load $P = P_0$ moves two rotations (MPa)
$\sigma_{\theta,T=1.5T_m}^{1.5P(0)\sim 1.5P(4\pi)}(\theta)$ Interface stress σ_θ under impact force $T = 1.5T_m$ due to the load $P = 1.5P_0$ moves two rotations (MPa)
σ_θ^{Res} Residual stress (MPa)
$\sigma_{\theta\,\mathrm{Rolling}}$ Rolling stress (MPa)
$\sigma_{\theta\,\mathrm{Res+Shrink}}$ Sum of residual stress and shrink-fitting stress (MPa)
σ_w Fatigue limit stress (MPa)
σ_{w0} Fatigue limit stress without defect (MPa)
σ_{w0}' Fatigue limit stress at the defect size $\sqrt{\mathrm{area}} = 627\mu m$ observed in miniature roll (MPa)
σ_{w0}'' Fatigue limit stress by considering real roll defect $\sqrt{\mathrm{area}} = 1254\mu m$ (MPa)
φ Load shift angle (°)
φ_0 Load shift interval (°)
$\updownarrow_{\mathrm{small}}$ The smaller contact stress region (MPa)
$\sqrt{\mathrm{area}}$ Projected area of the defect onto a plane perpendicular to the maximum principle stress
K_t Stress concentration
a, b, c Dimension of the defect in the miniature roll (μm)
r, θ, z Polar coordinate system
x, y, x Cartesian coordinate system

1 Introduction

In steel manufacturing industries, rolling processes more tonnage than any other metalworking process [1–22]. Among rolling rolls used in steel industries, sleeve assembly types whose shaft is shrink-fitted into a hollow cylinder have been tried to be used. Some of them have been successfully used as back-up rolls with a large body diameter exceeding 1000 mm and also as work rolls for large H-section steel. Figure 1 shows an example of the sleeve roll used as a real hot strip rolling roll. To express the high-speed steel (HSS)/ductile casting iron (DCI) rolls, several technical words such as bimetallic, composite, and compound are commonly used. In this article, "bimetallic" has been used similarly to our previous papers [18, 19]. By replacing the conventional single-material rolls, bimetallic work rolls are developed through improving wear resistance and heat crack

resistance [12–14]. Those sleeve rolls have several advantages. The shaft can be reused by replacing the sleeve after consumption due to the abrasion or the surface roughening. Furthermore, the sleeve wear resistance can be improved independently without loosening the shaft ductility. It should be noted that next generation rolls such as the super-cermet roll [15] and all ceramic roll [16] can be manufactured only as a sleeve roll. This is the reason why we have to develop sleeve roll technologies.

To develop this shrink-fitted sleeve roll, however, several peculiar problems have to be solved. They are known as residual bend deformation, fretting fatigue cracks at the sleeve end and sleeve fracture due to the circumferential sleeve slippage [5–11]. Among them, no detail studies are available for this circumferential slippage. Similar slippage is known as "interfacial creep" in ball bearing [23–35] although quantitative discussions are not available. Considering those situations, in the authors' previous studies, numerical simulation named load shifting method (see Fig. 2) was performed to realize the slippage by assuming a single material sleeve roll in Fig. 1A [17–21]. Note that the circumferential slippage usually occurs even though the resistance torque at the interface is larger than the motor torque. This is because non-uniform slip is caused by the loading although the conventional design only considers overall slip. The non-uniform slip often causes the fatal sleeve fracture in the following way [5, 6]. First, several scratches and partial seizures happen at the sleeve shrink-fitting surface. Second, the seizure growth causes surface roughness with a few millimeter depths. Third, due to the roughness, fatigue crack initiates and propagates at the sleeve inner surface causing the final fracture. In this way, the fatigue strength evaluation is necessary for sleeve rolls as well as clarifying the mechanism of interface slip.

In this study, the fatigue strength of the sleeve roll in Fig. 1 used in hot strip rolling mill will be discussed. According to the recent studies [50, 51], the fatigue strength of a bimetallic solid roll where no shrink-fitting should be investigated focusing on the debonding failures at HSS/DCI boundary due to the stress σ_r [5, 52] (see Fig. 15 in Appendix C). In this study, even in the case of the bimetallic sleeve roll in Fig. 1B, the interface slip at the shrink-fitted interface must be taken into account instead of the debonding failures at HSS/DCI boundary. Therefore, in this study, the fatigue strength will be analyzed by expanding the load shifting method, which can realize the accumulation of local slip. Instead of the relative slip displacement in the previous article, the fatigue-inducing stress amplitude will be focused in this simulation. It should be noted that the damage caused by the slip will be also considered as a defect reported in the previous studies. Then, the fatigue limit will be evaluated by applying the $\sqrt{\text{area}}$ parameter model to create a fatigue limit diagram and to evaluate the safety zone for the sleeve roll defects.

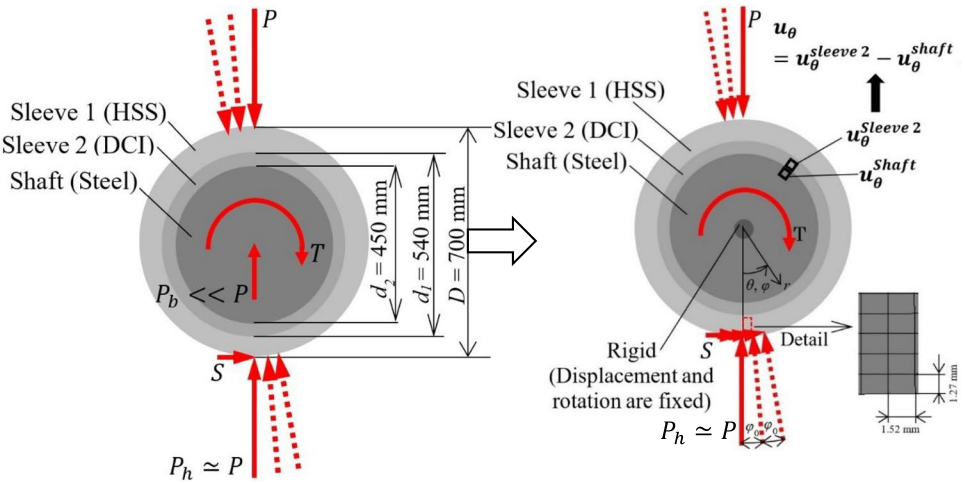

P: Load form back-up roll and hot strip (N)
S^*: Frictional force (N)
P_b^*: Bending force from bearing (N)
P_h: Rolling reaction force (N)
T: Driving torque (Nm), $T = SD/2$
T_m^*: Rated torque of motor (Nm)
T_r^*: Slippage resistance torque (Nm)
θ: Circumferential displacement angle
φ_0: Load shift interval
φ: Load shift angle

(A) Real roll. (B) Analysis roll model.

Fig. 2 Modelling for bimetallic sleeve roll

2 Interfacial slip simulation focusing on the interface stress σ_θ

In the previous studies [17–21], numerical simulations were performed to clarify the slippage by using a simplified rigid/elastic shaft in a single material sleeve roll as shown in Fig. 1A. Then, the amount of the slip was investigated by varying several design factors such as shaft deformation, motor torque, and shrink-fitting ratio. The outline of the load shifting method [17–21] is indicated in Appendix A where the roll rotation is replaced by the load shifting on the fixed roll.

Figure 1 illustrates a sleeve roll considered for the fatigue risk evaluation when it is used in the 4-stage rolling mill. In the sleeve roll shown in Fig. 1A, a steel shaft is shrink-fitted to a steel sleeve. Since the sleeve is required to have different properties, the bimetallic sleeve is used as the outer and inner layers. Figure 1B shows an example of a commonly used bimetallic sleeve roll manufactured by the centrifugal casting method. In Fig. 1B, a steel shaft is shrink-fitted to a sleeve roll consisting of a bimetallic sleeve. Here, a two-layer sleeve consists of the outer layer which is made of high-speed steel (HSS) having both wear resistance and toughness, and the inner layer is made of ductile casting iron (DCI) having high ductility.

As shown in Fig. 2, the roll is subjected to the contact force P from the back-up roll, the rolling reaction force P_h, and the frictional force S from the rolling plate. Since two-dimensional modelling is applied, the external force per unit length should be considered as well as motor torque T. In Fig. 1, the back-up roll is longer than the width of the rolling plate; and therefore, the bending force P_b is acting at the bearing. Here, the rolling force P, the rolling reaction force P_h, and the bending force P_b should be balanced, but P_b is estimated to be $< 10\%$ of P and P_h [5]. Therefore, in this study, assume the bending force $P_b = 0$; then, the rolling force ($=\sim P\times$ back-up roll body length) is equal to the rolling reaction force ($=\sim P_h\times$ strip width) as $P \simeq P_h$. This modelling refers to the case study of the loading at the fifth stage of hot finishing roll [5].

Figure 2 illustrates two-dimensional modelling in numerical simulation. Similar to Fig. 1, in Fig. 2, the two-layer sleeve and the steel shaft are shrink-fitted and the two-layer sleeve consists of HSS ans DCI. By applying the load shifting method [17–22], the roll rotation is expressed by the load shifting on the fixed roll surface. Figure 2A illustrates the real roll expressed by shifting the load on the roll surface with the roll center fixed. The roll is assumed to be subjected to the concentrated rolling load P. In the rolling process, the friction S is used to compress the rolling plate between the rolls as well as the driving torque T from the motor to the shaft. Figure 2B is the model used in this study when the bending force $P_b = 0$ is assumed. A rigid body is introduced at the center of the shaft to restrain the displacement and rotation of the center of the roll. It is confirmed that the rigid body size at the center does not affect the result, and the diameter 8 mm is used. Figure 2B also shows an example of the mesh division for the finite element method (FEM).

Heating and cooling from the hot-rolled steel sheet generate thermal stress during one rotation of the roll. However, thermal stress affects only a few μm to 1 mm depth from the surface, and does not affect internal stress at all [30, 54–58]. After the start of rolling, the roll temperature rises and stabilizes at the equilibrium temperature of 50–80 °C after 1 h [5, 30, 54–58]. Rolling is continued for more than 10 h until the damaged roll surface needs to be removed, so the effects of thermal stress in the early stages of rolling are relatively small and can be ignored when considering fatigue strength.

Recently, the fatigue strength of a bimetallic solid roll was estimated whose fatigue risk was considered in the previous paper [50, 51]. In the solid bimetallic roll, it was reported that the failures happened as the debonding at HSS/DCI boundary due to the stress σ_r as well as the roll center facture [5, 52]. Figure 15 in Appendix C shows a bimetallic solid roll whose fatigue risk was considered in the previous paper [50, 51]. In the solid bimetallic roll, it was reported that the failures happened as the debonding at HSS/DCI boundary due to the stress σ_r as well as the roll center facture [5, 52]. The finite element method (hereinafter abbreviated as FEM) is used for the numerical analysis of the sleeve assembly type roll in Fig. 2. To realize the interface slippage, the FEM simulation should be well conducted on basis of the experience and skills for engineering applications. In the previous studies [36–39], the FEM mesh error was discussed for bonded problems and the mesh-independent technique was proposed confirming that the displacement boundary condition applied is relatively insensitive. Contact status change was clarified when the pitch-difference nut is tightened [40] and dynamic deformation was investigated through consecutive quasi-static analyses [41]. On the basis of those skills, during the ceramic roll rotation, the axial movement of the shaft was analyzed by shifting the load on the fixed shaft [42–45]. In this study, the circumferential sleeve slippage will be realized by extending the above technique and applying FEM code Marc/Mentat 2012 to the elastic contact quasi-static analysis for rolling rolls. In this code, the complete Newton–Raphson method and the direct constraint method for the contact analysis are used. As shown in Fig. 2B, a 4-node quadrilateral plane strain is used with the number of mesh elements are $3.\times 10^5$ with confirming the mesh independency of the results [46].

Table 1 shows the roll dimensions considered in this paper as a standard roll. Table 1 also indicates mechanical properties, and boundary conditions used in the analysis. In

Table 1 Dimensions, mechanical properties, and boundary conditions in Fig. 1B considered as a standard roll in this study

Mechanical properties	Sleeve	Shell E_{sleeve}	233 GPa
		ν_{sleeve}	0.3
		Core E_{sleeve}	173 GPa
		ν_{sleeve}	0.3
	Shaft	E_{shaft}	210 GPa
		ν_{shaft}	0.28
Roll size		Outer diameter of sleeve D	700 mm
		Inner diameter sleeve d_1	540 mm
		Inner diameter sleeve d_2	450 mm
Shrink-fitting		Shrink-fitting ratio δ/d	0.5×10^{-3}
		Friction coefficient between sleeve and shaft μ	0.3
External force		Concentrated load per unit width $P = P_0$	13,270 N/mm (Total: 1.327 × 107 N; Rolled width: 1000 mm)
		Frictional force per unit width S	1346 N/mm
		Motor torque per unit width T_m	471 Nm/mm
		Resistance torque per unit width T_r	3193 Nm/mm
		Bending force from bearing P_b	0 N/mm

this study, the standard compressive force P is $P = P_0$ and the standard drive torque is $T = T_m$. The loading condition used in this study is based on the data at No. 5 stand for roll hot strip finishing roll mill [4, 5]. Assume conditions equivalent to hot rolling of ordinary steel sheets, a standard load $P = P_0 = 13270$ N/mm per 1 mm of roll is used. Small effect can be confirmed by replacing Hertzian contact stress with the concentrated force P. Instead of the standard force $P = P_0$ with the standard drive torque $T = T_m$, this study focuses on the rolling load $P = 1.5P_0$ with the drive torque $T = 1.5T_m$, which is corresponding to the impact load when the rolled plate biting trouble occurs.

The shrink-fitting ratio is defined as δ/d, where δ is the diameter difference between the inner diameter of the sleeve and the outer diameter of the shaft. Usually, the shrink-fitting ratio in the range $\delta/d = 0.4 \times 10^{-3} \sim 1.0 \times 10^{-3}$ is applied to sleeve rolls on the basis of long year experience. This is because a smaller value $\delta/d < 0.4 \times 10^{-3}$ may cause the interface to slip easily and a larger value $\delta/d > 1.0 \times 10^{-3}$ may increase the risk of sleeve fracture [6]. To study the irreversible interfacial slip, in this paper, $\delta/d = 0.5 \times 10^{-3}$ is focused. The effect of the shrink-fitting ratio has been discussed [18]. Regarding the friction coefficient μ controlling the slippage resistance at the interface, $\mu = 0.2$ was used in an experimental study and $\mu = 0.4$ was often used for steel surfaces previously [1, 47]. In this way, since $\mu = 0.2 \sim 0.4$ is usually used for sleeve assembly type rolls, in this study, the friction coefficient $\mu = 0.3$ between the sleeve and the shaft is used.

In the following sections, first, the displacement $u_\theta^{P(0)\sim P(\varphi)}(\theta)$ at the shrink-fitted interface obtained by the load shifting method will be shown (see Appendix A). This is the relative displacement between the sleeve and the shaft $(= u_{\theta,\text{sleeve}}^{P(0)\sim P(\varphi)}(\theta) - u_{\theta,\text{shaft}}^{P(0)\sim P(\varphi)}(\theta))$ due to the load shifting $P(0) \sim P(\varphi)$. The interface slip can be regarded as the accumulation of $u_\theta^{P(0)\sim P(\varphi)}(\theta)$. If such accumulated slip occurs in a real rolling roll, several scratches and partial seizures happen at the shrink-fitted surface may cause crack initiation, crack propagation, and final sleeve fracture [6]. Considering such failure, the stress σ_θ causing such damage at the shrink-fitted surface will be focused instead of the debonding stress σ_r at HSS/DCI boundary regarding the solid bimetallic roll. Therefore, the stress $\sigma_\theta^{P(0)\sim P(\varphi)}(\theta)$ at the shrink-fitted interface will be focused in the following sections in a similar way of the displacement $u_\theta^{P(0)\sim P(\varphi)}(\theta)$ in the previous papers.

3 Simulation results of rolling stress generated on the inner surface of the sleeve

3.1 *Rolling stress σ_θ at the inner surface of the sleeve*

In the sleeve roll, the circumferential slippage sometimes occurs even though the resistance torque at the interface is larger than the motor torque. In the previous studies, the interfacial slip was realized by the load shifting method described in Appendix A.

Figure 3A shows the interfacial slip $u_{\theta,T=T_m}^{P(0)}(\theta)$, which is the relative displacement u_θ at $\theta = \theta$ when the standard drive torque is $T = T_m$ and the initial load $P = P_0$ is applied at $\varphi = 0$ as $P(0)$. Fig. 3A also shows $u_{\theta,T=T_m}^{P(0)\sim P(2\pi)}(\theta)$, which is the circumferential displacement u_θ when the standard rolling condition $P = P_0, T = T_m$ moves from $\varphi = 0$ to $\varphi = 2\pi$ as

Fig. 3 Interface displacement $u^{P(0)}_{\theta,T=T_m}$ in Fig. 1B due to the initial load $P = P_0$ increases as can be expressed $u^{P(0)}_{\theta,T=T_m} < u^{P(0)\sim P(2\pi)}_{\theta,T=T_m} < u^{P(0)\sim P(4\pi)}_{\theta,T=T_m}$ by shifting the load as $P(0) \sim P(2\pi) \sim P(4\pi)$ but interface stress distributions remains the same as can be expressed by $\sigma^{P(0)\sim P(2\pi)}_{\theta,T=T_m}(\theta) \approx \sigma^{P(0)\sim P(4\pi)}_{\theta,T=T_m}(\theta)$

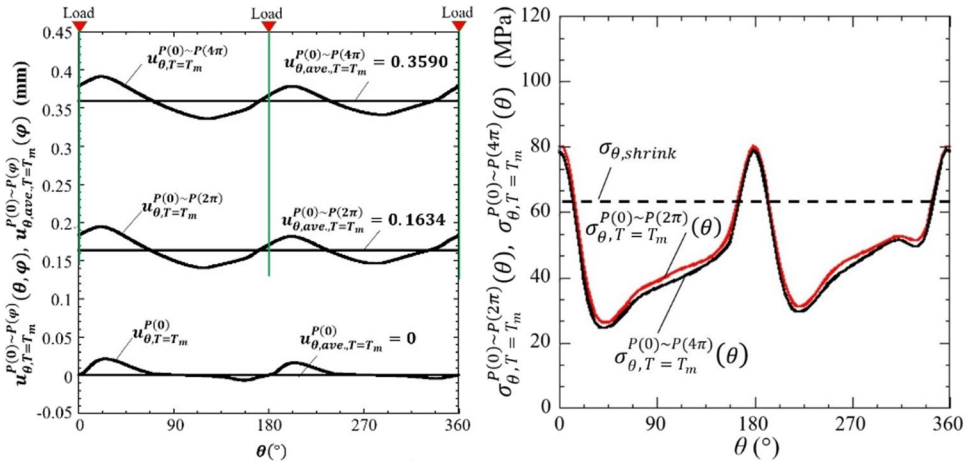

(A) Circumferential interface displacement distribution increases as $u^{P(0)}_{\theta,T=T_m} < u^{P(0)\sim P(2\pi)}_{\theta,T=T_m} < u^{P(0)\sim P(4\pi)}_{\theta,T=T_m}$.

(B) Circumferential interface stress distribution remains as $\sigma^{P(0)\sim P(2\pi)}_{\theta,T=T_m}(\theta)$ and $\sigma^{P(0)\sim P(4\pi)}_{\theta,T=T_m}(\theta)$.

$P(0) \sim P(2\pi)$. Fig. 3A also shows $u^{P(0)\sim P(4\pi)}_{\theta,T=T_m}(\theta)$ when the standard rolling condition $P = P_0, T = T_m$ moves two rotations as $P(0) \sim P(4\pi)$. As shown in Fig. 3A, the displacement $u^{P(0)\sim P(\varphi)}_{\theta,T=T_m}(\theta)$ increases with increasing φ. Since the displacement $u^{P(0)\sim P(\varphi)}_{\theta,T=T_m}(\theta)$ varies depending on θ, the average displacement can be defined in Eq. (1).

$$u^{P(0)\sim P(\varphi)}_{\theta,ave.,T=T_m} = \frac{1}{2\pi}\int_0^{2\pi} u^{P(0)\sim P(\varphi)}_{\theta,T=T_m}(\theta)d\theta \tag{1}$$

As shown in Fig. 3A, more clearly, the average displacement $u^{P(0)\sim P(\varphi)}_{\theta,ave.,T=T_m}$ increases due to the load shifting from $\varphi = 0$ to $\varphi = 4\pi$.

If such circumferential slip $u^{P(0)\sim P(\varphi)}_{\theta,T=T_m}(\theta)$ occurs in a real rolling roll, several scratches and partial seizures happen at the sleeve shrink-fitting surface. Then, the seizure growth with the roll rotation causes the surface roughness with a few millmeter depths. Due to the roughness, fatigue crack initiates and propagates at the sleeve inner surface causing the final fracture [6]. Considering such failure, the stress σ_θ at the shrink-fitted surface is focused in this paper since σ_θ is the largest stress component and causes such damage. The stress $\sigma^{P(0)\sim P(\varphi)}_{\theta}(\theta)$ is defined as the interface stress σ_θ due to the load shifting $P(0) \sim P(\varphi)$ from the angle $\varphi = 0$ ($\varphi = \pi$) to $= \varphi$ ($\varphi = \varphi + \pi$). Here, notation φ denotes the angle where the load is shifting and notation θ denotes the position where the stress is considered.

Figure 3B shows the stress distribution, $\sigma^{P(0)\sim P(2\pi)}_{\theta,T=T_m}(\theta)$, which is the stress σ_θ when the load $P = P_0$ moves one rotation as $P(0) \sim P(2\pi)$. Figure 3B also shows $\sigma^{P(0)\sim P(4\pi)}_{\theta,T=T_m}(\theta)$ when the load $P = P_0$ moves two rotations as $P(0) \sim P(4\pi)$. As shown in Fig. 3B, no large difference between σ_θ after one rotation and σ_θ after two rotations of the load P. In other words, the accumulation phenomenon observed in the displacement is not seen in the stress. For the fatigue risk evaluation, therefore, the stress obtained after two rotations can be always used irrespective of the number of the roll rotation.

Figure 4 shows the stress distribution along the interface $\sigma^{P(0)\sim P(4\pi)}_{\theta,T=T_m}(\theta)$ when the load $P = P_0$ moves two rotations as $P(0) \sim P(4\pi)$ in comparison with the stress distribution $\sigma^{1.5P(0)\sim 1.5P(4\pi)}_{\theta,T=1.5T_m,}(\theta)$ when the load $P = 1.5P_0$ moves as $P(0) \sim P(4\pi)$. Under the load $P = P_0$, the maximum stress is $\sigma^{P_0}_{\theta\max} = 79.4$ MPa and the minimum stress is $\sigma^{P_0}_{\theta,\min} = 24.6$ MPa. On the other hand, under the load $P = 1.5P_0$, which is corresponding to the impact load when the rolled plate biting trouble occurs, the maximum stress is $\sigma^{1.5P_0}_{\theta,\max} = 91.3$ MPa and the minimum stress is $\sigma^{1.5P_0}_{\theta\min} = -24.7$ MPa. Here, the stress amplitude σ_a and the mean stress σ_m are expressed in Eqs. (2) and (3).

$$\sigma_a = \left(\sigma_{\theta\max} - \sigma_{\theta\min}\right)/2 \tag{2}$$

$$\sigma_m = \left(\sigma_{\theta\max} + \sigma_{\theta\min}\right)/2 \tag{3}$$

For the stress σ_θ under the load $P = P_0$, the stress amplitude is $\sigma_a = 27.4$ MPa and mean stress is $\sigma_m = 52.0$ MPa. On the other hand, under the load $P = 1.5P_0$, the stress amplitude is $\sigma_a = 58.0$ MPa and mean stress is $\sigma_m = 33.3$ MPa. This observation shows that by considering the impact force $P = 1.5P_0$, the stress amplitude σ_a is about 2.1 times, and the mean stress σ_m is about 0.6 times from the stress under the standard condition $P = P_0$.

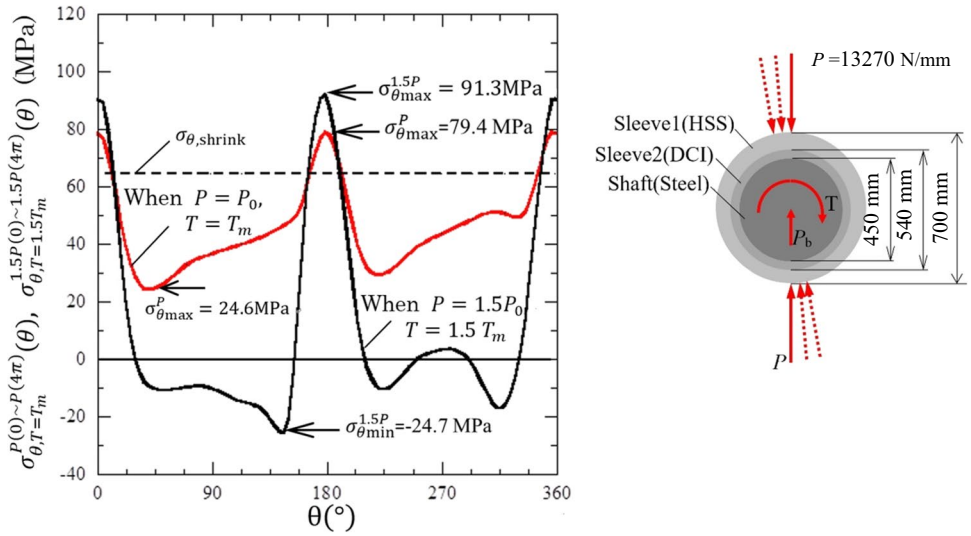

Fig. 4 Circumferential interface stress distribution $\sigma^{P(0)\sim P(4\pi)}_{\theta,T=T_m}(\theta)$ in Fig. 1B under standard loading condition $P=P_0$ and $T=T_m$ in comparison with $\sigma^{1.5P(0)\sim 1.5P(4\pi)}_{\theta,T=1.5T_m}(\theta)$ under impact loading condition $P=1.5P_0$ and $T=1.5T_m$. Under the impact force $P = 1.5P_0$, the stress amplitude σ_a is about 2.1 times larger than the stress under the standard load $P = P_0$

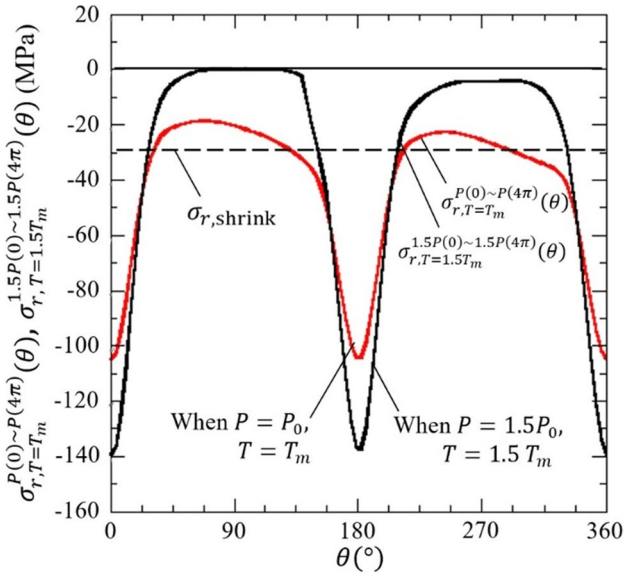

Fig. 5 Radial interface stress distribution $\sigma^{P(0)\sim P(4\pi)}_{r,T=T_m}(\theta)$ in Fig. 1B under standard loading condition $P=P_0$ and $T=T_m$ in comparison with $\sigma^{1.5P(0)\sim 1.5P(4\pi)}_{r,T=1.5T_m}(\theta)$ under impact loading condition $P=1.5P_0$ and $T=1.5T_m$. The smaller contact stress region $\updownarrow_{small}$ satisfying $\sigma_r^{P(0)\sim P(4\pi)} \leqq \sigma_{r_{\text{shrink}}}$ is larger under impact loading condition

3.2 *Contact stress σ_r at the inner surface of the sleeve*

Previously the authors found the smaller contact stress region where the slip is promoted [19]. The smaller contact stress region $\updownarrow_{small}$ is a region where the contact stress $\sigma^{P(0)\sim P(\varphi)}_{r,T=T_m}$ becomes smaller than the original shrink-fitted stress $\sigma_{r_{\text{shrink}}}$ as $\sigma_r^{P(0)\sim P(4\pi)} \leqq \sigma_{r_{\text{shrink}}}$. Here, $\sigma_{r_{\text{shrink}}}$ denotes the shrink-fitting stress without applying the load P.

Figure 5 shows the stress distribution $\sigma^{P(0)\sim P(4\pi)}_{r,T=T_m}(\theta)$ when the load $P = P_0$ moves as $P(0) \sim P(4\pi)$ in comparison with the stress distribution $\sigma^{1.5P(0)\sim 1.5P(4\pi)}_{r,T=1.5T_m}(\theta)$ when the load $P = 1.5P_0$ moves as $P(0) \sim P(4\pi)$. As shown in Fig. 5, the smaller contact stress region $\updownarrow_{\text{small}}$ can be confirmed under the standard condition $P = P_0, T = T_m$ and also under the impact force condition $P = 1.5P_0, T = 1.5T_m$. In addition, with increasing the load from $P = P_0, T = T_m$ to $P = 1.5P_0, T = 1.5T_m$, the smaller contact stress region $\updownarrow_{\text{small}}$ increases. It should be noted that under the condition of $P = 1.5P_0, T = 1.5T_m$, the zero contact stress region appears as $\sigma^{1.5P(0)\sim 1.5P(4\pi)}_{r,T=1.5T_m} \cong 0$ around $\theta = 90^{\circ}$ where the sleeve and the shaft is separated. This region can be named the non-contact region. It may be concluded that under high load conditions, the non-contact region appears and accelerates the slippage.

To clarify the separation condition, Fig. 6 shows $\sigma^{P(0)\sim P(4\pi)}_{r,T=T_m}(\theta)$ by varying the load from the standard condition $P = P_0, T = T_m$ to the impact force condition $P = 1.5P_0, T = 1.5T_m$. It was found that the separation occurs when $P/P_0 \geq 1.5$ and $T/T_m \geq 1.5$. Under the larger load $P/P_0 \geq 1.5$ and $T/T_m \geq 1.5$, the stress amplitude becomes much larger.

3.3 Residual stress and shrink-fitting stress

Based on the rolling stress $\sigma_\theta^{\text{Rolling}}$ obtained in the above discussion, the fatigue failure risk can be evaluated considering the crack initiation from the inner surface of the sleeve. In the real roll, however, when the sleeve roll is manufactured, the residual stress due to heat treatment is introduced. In the previous study [22], the residual simulation was performed during quenching and tempering for the conventional bimetallic solid rolls. In a similar way, the residual simulation is performed for the bimetallic sleeve roll in Fig. 1B to obtain the residual stress in Fig. 7B.

Figure 7A shows the residual stress distribution σ_θ^{Res} at the central cross section z = 0 after the quenching and

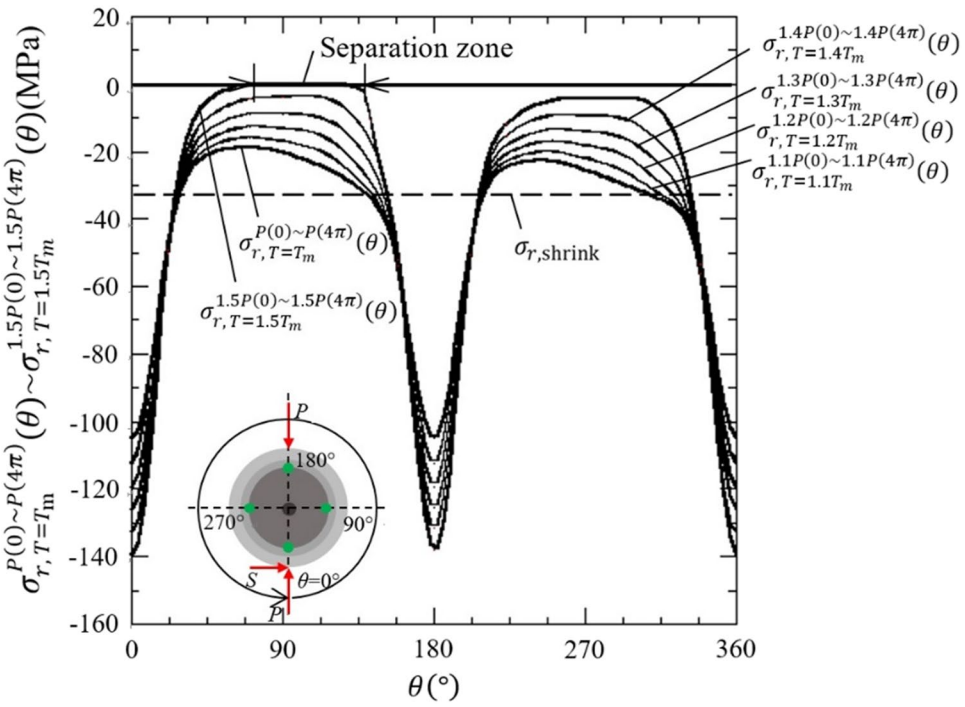

Fig. 6 Radial interface stress distribution $\sigma_{r,T=T_m}^{P(0)\sim P(4\pi)}(\theta)$ in Fig. 1B when the rolling load P and the driving torque T are changed at the same time in the range $P=P_0\sim1.5\,P_0$ and $T=T_m\sim1.5T_m$. The separation zone where $\sigma_{r,T=T_m}^{P(0)\sim P(4\pi)}(\theta)=0$ appears at the shrink-fitted surface when $P/P_0\geq1.5$ and $T/T_m\geq1.5$

tempering before the shrink-fitting. This is the results obtained from heat treatment analysis as shown in the previous study [22]. Figure 7B shows the stress distribution obtained by superposing the residual stress and the shrink-fitting stress as $\sigma_\theta^{\mathrm{Res+Shrink}}$ at $z=0$ after the shrink-fitting.

As shown in Fig. 7B, the residual stress distribution after shrink-fitting the shaft has the maximum tensile stress $\sigma_\theta^{\mathrm{Res+Shrink}}=156$ MPa at r = 225 mm of the sleeve. In the next section, the fatigue strength will be discussed by considering the superposition of residual stress and the shrink-fitting stress as $\sigma_\theta^{\mathrm{Res+Shrink}}$ [22] and the rolling stress $\sigma_\theta^{\mathrm{Rolling}}=\sigma_{\theta,T=1.5T_m}^{1.5P(0)\sim1.5P(4\pi)}(\theta)$ at the inner surface of the sleeve in Fig. 4. In this evaluation, the stress σ_θ at the sleeve interface is focused since the stress σ_θ mainly controls the crack initiation.

4 Fatigue strength evaluation for the sleeve roll considering slip defect by using the stress amplitude versus mean stress diagram ($\sigma_a-\sigma_m$diagram)

In this section, the fatigue strength of the sleeve roll in Fig. 1B is evaluated on the basis of the rolling stress $\sigma_\theta^{\mathrm{Rolling}}$ in Section 3.1 obtained by the load shifting method. In

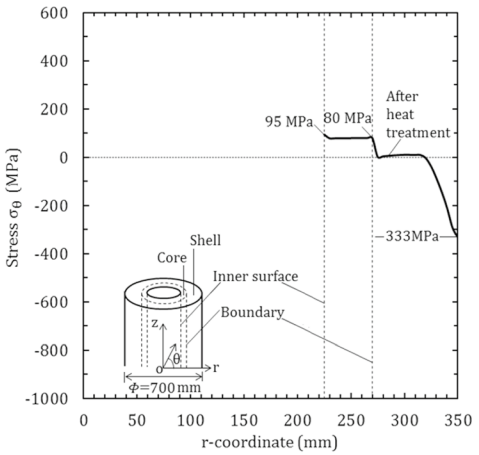

(A) Residual stress σ_θ distribution before shrink-fitting.

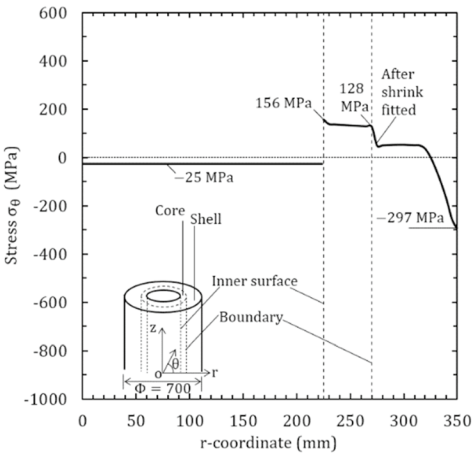

(B) Residual and shrink-fitting stress σ_θ after shrink-fitting.

Fig. 7 Circumferential residual stress distribution σ_θ at the central cross section z = 0 in Fig. 1B obtained through sleeve heat treatment

the authors' recent study, the validity of this simulation was confirmed through the experiment by using a miniature roll [48, 59]. Then, the slippage and the defect were experimentally identified at the sleeve/shaft surfaces as shown in Appendix B. Therefore, in the present study, the fatigue strength should be analyzed considering the defect geometries identified as well as $\sigma_\theta^{\text{Rolling}}$. The rolling stress $\sigma_\theta^{\text{Rolling}}$ can be clasified into the stress amplitude and the mean stress. The stress amplitude-mean stress diagram is used to characterize the effect of mean stress to assess the fatigue strength of metals. Mean stress is known to greatly affect fatigue strength.

During rotation, the bimetallic solid rolls are also cyclically loaded with compressive mean stress (see Appendix C). In this case, since there is no shrink-fit or slip damage, the fatigue strength was analyzed focusing on the debonding commonly observed at the HSS/DCI interface [5, 51–53]. Then, stress amplitude versus mean stress diagrams (σ_a-σ_m diagram) were considered under large compressive alternative loads $\sigma_m \leq 0$[50]. Unlike solid rolls, the σ_a-σ_m diagram of sleeve rolls must consider the reduction in fatigue strength due to slip defects. Regarding the fatigue limit for the engineering material having some defects, Eq. (4) is proposed for the stress ratio range $-1 \leq R \leq 0$ [49],

$$\sigma_w = \frac{1.43(H_V+120)}{\left(\sqrt{\text{area}}\right)^{1/6}}\left[\frac{1-R}{2}\right]^{\alpha},\ R = \frac{\sigma_{\theta\min}}{\sigma_{\theta\max}} \tag{4}$$

where H_V (kgf/mm^2) is the Vickers hardness of DCI and area is the projected area of the defect.

In the previous study, the slip defect geometry was identified by using a miniature rolling mill whose dimension about 1/10 of standard sleeve roll in Fig. 1B. Based on the miniature roll experiment (see Appendix B), the slip defect size can be characterized by $\sqrt{\text{area}} = 627\mu m$ [48, 59]. Figure 8A illustrates the DCI inner layer fatigue limit obtained from Eq. (4) as curve AB when $\sqrt{\text{area}} = 627\mu m$. Since Eq. (4) is proposed based on data in the range $-1 \leq R \leq 0$, the curve AB is indicted for $R = -1 \sim 0$ in Fig. 8A where point A corresponds to the fatigue limit of fully reversed loading $R = -1$ with defect size $\sqrt{\text{area}}$=627 μm. Point B can be determined as the intersection of the curve obtained from Eq. (4) and the straight line $\text{R} = \left(\sigma_m/\sigma_a - 1\right)/\left(\sigma_m/\sigma_a + 1\right) = -1$. Point B corresponds to the fatigue limit of pulsating tensile load R = 0 with defect size $\sqrt{\text{area}}$=627 μm.

Figure 8B illustrates the DCI inner layer fatigue limit as a straight line BC when the defect size is characterized by $\sqrt{\text{area}} = 627\mu m$. Point C corresponds to the tensile strength of the DCI $\sigma_B = 415$ MPa, which is independent of the slip defect dimension. Recently, Ikeda et al. clarified that the strength of the circumferential notched specimen is larger than the strength of the plain specimen for the wide range of tensile speed and temperature [53]. Therefore, the static strength of DCI including some defects can be the same as the tensile strength of the DCI without defects $\sigma_B = 415$ MPa. In this way, in the range $R \geq 0$, the straight line BC can be used as the fatigue limit line.

Figure 9A shows the fatigue limit ABC explained above where the defect size $\sqrt{\text{area}} = 627\mu m$ in comparison with the common fatigue limit line DC for DCI with no defect. Point D corresponds to the fatigue limit of fully reversed loading $R = -1$ when DCI has no slip defect. Then, the rolling stress $\sigma_\theta^{\text{Rolling}}$ under the impact force condition $P = 1.5P_0, T = 1.5T_m$ are considered. In Fig. 9A, point E shows stress amplitude and mean stress (σ_a, σ_m) due to the rolling stress $\sigma_\theta^{\text{Rolling}}$ and shrink-fitting stress $\sigma_\theta^{\text{Shrink}}$. Point F shows stress amplitude and mean stress (σ_a, σ_m) due to the rolling stress $\sigma_\theta^{\text{Rolling}}$, shrink-fitting stress $\sigma_\theta^{\text{Shrink}}$, and residual stresses σ_θ^{Res}. Here, the mean stress is obtained by superposing those stresses as $\sigma_\theta^{\text{Res+Shrink}} + \sigma_\theta^{\text{Rolling}} = 189.3$ MPa.

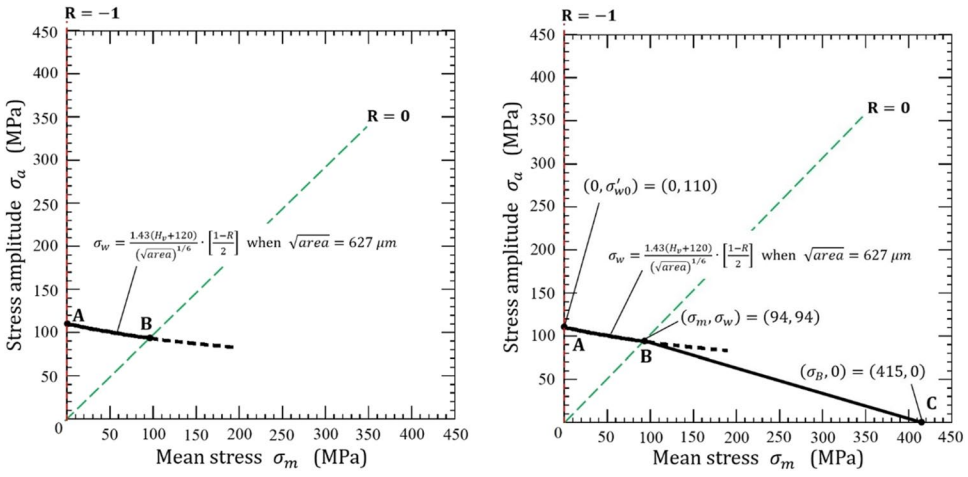

(A) Fatigue limit estimation for DCI with the defect size $\sqrt{area} = 627\ \mu$m.

(B) Fatigue limit for DCI with the defect size $\sqrt{area} = 627\ \mu$m.

Fig. 8 Estimation of the fatigue limit of DCI with defect size $\sqrt{\text{area}} = 627\mu m$. Point A: Fatigue limit of fully reversed loading R = −1 with defect size $\sqrt{\text{area}}$=627 μm; Point B: Fatigue limit of pulsating tensile loading R = 0 with defect size $\sqrt{\text{area}}$=627 μm; Point C: Ultimate tensile strength independent of the defect size

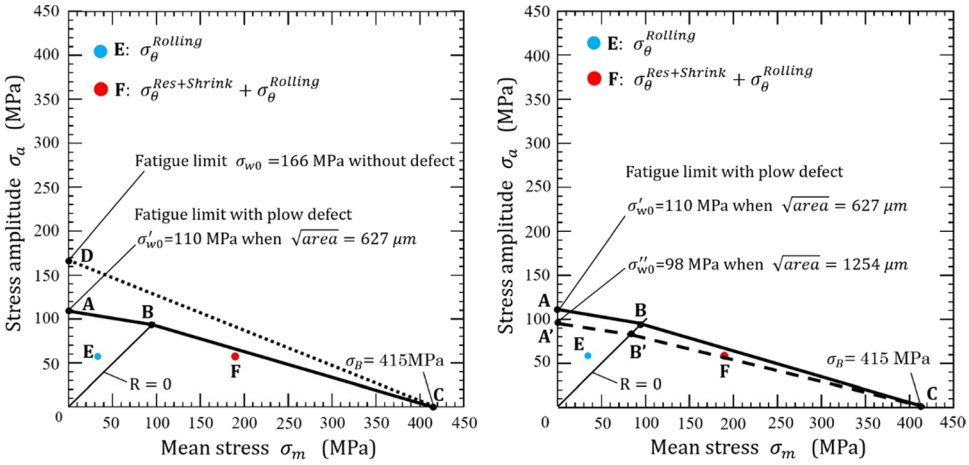

(A) Fatigue limit diagram to evaluate two critical points.

(B) Fatigue limit diagram by considering the real roll defect $\sqrt{area}$=1254 μm.

Fig. 9 Stress amplitude σ_a versus mean stress σ_m diagram for σ'_{w0} = 110 MPa when $\sqrt{\text{area}}$=627 μm, σ''_{w0} = 98 MPa when $\sqrt{\text{area}}$=1254 μm and σ_B = 415 MPa. Point A: Fatigue limit of fully reversed loading R = −1 with defect size $\sqrt{\text{area}}$=627 μm; Point B: Fatigue limit of pulsating tensile loading R = 0 with defect size $\sqrt{\text{area}}$=627 μm; Point C: Tensile strength independent of the defect size; Point D: Fatigue limit of fully reversed loading without defect; Point A′: Fatigue limit of fully reversed loading R = −1 with defect size $\sqrt{\text{area}}$ =1254 μm; Point B′: Fatigue limit of pulsating tensile loading R = 0 with defect size $\sqrt{\text{area}}$=1254 μm; Point E: Plot (σ_a, σ_m) due to the rolling and shrink-fitting stresses; Point F: Plot (σ_a, σ_m) due to the rolling, shrink-fitting, and residual stresses

In Appendix B, as well as the previous miniature roll experiment, the slip defect dimensions in the standard sleeve roll in Fig. 1B is estimated. The standard roll diameter in Fig. 1B is about 10 times larger than the miniature roll. The defect size found in the experimental study $\sqrt{\text{area}} = 627\mu\text{m}$ may be smaller for the standard roll in Fig. 1B. Therefore, the double sizes of the defect with $\sqrt{\text{area}} = \sqrt{\pi(2a)(2b)/2}$ $=627 \times 2 = 1254\ \mu m$ may be suitable. Here, the previous report for the roll much larger than Fig. 1B was also considered [5, 6]. In Fig. 9B, point A′ corresponds to the fatigue limit of fully reversed loading R = −1 with defect size $\sqrt{\text{area}}$ =1254 μm. Point B′ corresponds to the fatigue limit of pulsating tensile load $R = 0$ with defect size $\sqrt{\text{area}}$=1254 μm. If the fatigue limit A′B′C is used, point F is located on the slightly dangerous side.

The fatigue failure risk of the bimetallic solid roll studied in the recent paper is indicated in Appendix C [50, 51]. In the solid bimetallic roll, since the failures happened as the debonding at HSS/DCI boundary [5, 52], the risk of fatigue failure was evaluated focusing on the stress σ_r. The results show that if there is no slip damage, the fatigue strength of the sleeve roll is not very smaller compared to the fatigue strength of the solid roll with no shrink-fitting (see Fig. 9A, Fig. 7A). If the interfacial slip can be prevented by providing a key between the sleeve and the shaft for example, the risk of fatigue can be the same of the solid bimetallic roll.

In this paper, the fatigue strength of the standard sleeve roll in Fig. 1B was evaluated. The detail of the sleeve roll in Fig. 1B was indicated in Table 1. First, the slip defect geometry observed in the miniature roll experiment was considered. The detail of the miniature roll experiment was indicated in Fig. 12 and Table 2. The detail of the slip geometry was indicated in Fig. 13 and Fig. 14, which can be characterized by the root area parameter $\sqrt{\text{area}} = 627$ μm. Then, the fatigue limit in the stress amplitude-mean stress diagram is indicated in Fig. 9A. The plot in Fig. 5 is obtained by applying the load shifting method realizing the local slip accumulation during roll rotation. Next, the slip defect geometry in the real roll in Fig. 1B was estimated as shown in Appendix B obtained as $\sqrt{\text{area}} = 1254$ μm. Then, the fatigue limit is indicated in Fig. 9B. The fatigue risk is discussed comparing to the solid roll where there is no shrink-fit as in Fig. 16 of Appendix C.

5 Conclusions

Toward developing next generation rolls such as supercermet rolls, the fatigue strength of the sleeve roll was considered in this paper. Considering the circumferential slippage appearing at the shrink-fit interface, the load shifting method was applied on the fixed roll to clarify the stress variation during roll rotation. Based on this simulation results, the fatigue strength of standard rolling rolls is estimated considering the slip defect. The defect dimension was characterized by the root area parameter $\sqrt{\text{area}}$. The conclusions can be summarized in the following way:

- By applying the load shifting method, the roll rotation and the interface slip were realized. Then, the maximum stress, the minimum stress, and stress amplitude at the interface were clarified when the slip occurs at the shrink-fitted interface. It was found that the stress variation remains stable after one rotation (see Fig. 3) although the interfacial displacement increases with increasing the roll rotation.
- Under the impact loading conditions $P = 1.5P_0$ when the rolled plate biting trouble occurs, the stress amplitude becomes about twice larger than the stress under the standard loading conditions $P = P_0$ (see Fig. 4). This is because with increasing the load P, the smaller contact stress region where $\sigma_r^{P(0)\sim P(4\pi)} \leqq \sigma_{r_{shrink}}$ increases (see Fig. 5) and the separation zone where $\sigma_{r,T=1.5T_m}^{1.5P(0)\sim 1.5P(4\pi)} \cong 0$ appears (see Fig. 6).
- On the stress amplitude—mean stress diagram, the fatigue limit was expressed by considering the slip defect. From the miniature roll experiment and the previous report, the defect dimension was characterized by the root area parameter $\sqrt{\text{area}} = 1254\,\mu m$. Then, the fatigue failure risk of the bimetallic sleeve assembly type roll was evaluated on the basis of the stress variation obtained by the load shifting simulation under impact loading condition. It may be concluded that if there is no slip damage, the fatigue strength of the sleeve roll is not very smaller compared to the fatigue strength of the solid roll with no shrink-fitting (see Fig. 9A, Fig. 7A).

Appendix A: Load shifting method to realize the relative interfacial displacement $u_\theta^{P(0)\sim P(\varphi)}(\theta)$ and average interfacial displacement $u_{\theta,ave.}^{P(0)\sim P(\varphi)}(\theta)$

Figure 10 illustrates the load shifting method where the roll rotation is expressed by the load shifting on the fixed roll surface [17–21]. Assume the roll subjected to the concentrated rolling load P. As shown in Fig. 10, the continuous roll rotation can be expressed by the discrete load shifting with a constant interval φ_0. The most suitable value of φ_0 can be chosen to reduce the computational time without loosening the accuracy. From the comparison among the results $\varphi_0 = 0.25° \sim 12°$, the load shift angle $\varphi_0 = 4°$ is adopted in the following discussion since the relative error between $\varphi_0 = 0.25°$ and $\varphi_0 = 4°$ is less than a few percent. In the following, both forces are denoted by P.

The relative displacement accumulation between the sleeve and shaft may represent the interfacial slip. In Fig. 11, the relative displacement $u_\theta^{P(0)\sim P(\varphi)}(\theta)$ due to the load shifting $P(0) \sim P(\varphi)$ is defined between the sleeve and shaft when the load moves from the angle $\varphi = 0$ to $\varphi = \varphi$. Here, notation φ denotes the angle where the load is shifting and notation θ denotes the position where the displacement is evaluated. The load $P(\varphi)$ is defined as the pair of forces acting at $\varphi = \varphi$ and $\varphi = \varphi + \pi$. The notation $u_\theta^{P(0)\sim P(\varphi)}(\theta)$ means the relative displacement $u_\theta(\theta)$ at $\theta = \theta$ when the pair of loads are applied at $\varphi = 0$ to $\varphi = \varphi$ and $\varphi = \pi$ to $\varphi = \varphi + \pi$. Since the relative displacement $u_\theta(\theta)$ varies depending on θ, the average displacement $u_{\theta,ave.}^{P(0)\sim P(\varphi)}$ can be defined in Equation (A1).

$$u_{\theta,ave.}^{P(0)\sim P(\varphi)} = \frac{1}{2\pi}\int_0^{2\pi} u_\theta^{P(0)\sim P(\varphi)}(\theta)d\theta \tag{A1}$$

Appendix B: Estimation of slip defect dimension in standard sleeve roll in Fig. 1B

Figure 12(a) illustrates the real roll at the central cross section in Fig. 1B in comparison with Fig. 12(b) the miniature roll to verify the slippage experimentally [20, 48]. The miniature roll's diameter is about 1/10 of the real roll. As shown in Fig. 12(b), the miniature roll consists of the sleeve, the outer shaft and the inner shaft. The inner and outer shafts are fixed by key so that the interfacial slippage between the outer shaft and the sleeve shrink-fitted can be prevented.

Figure 13 shows an example of the defect observed on the sleeve surface after slippage. The sleeve is cut along the cross section at the AA′ and BB′ to identify the defect dimensions. Figure 14 illustrates the three dimensional shape of the defect approximated by an ellipsoid. As can be expressed

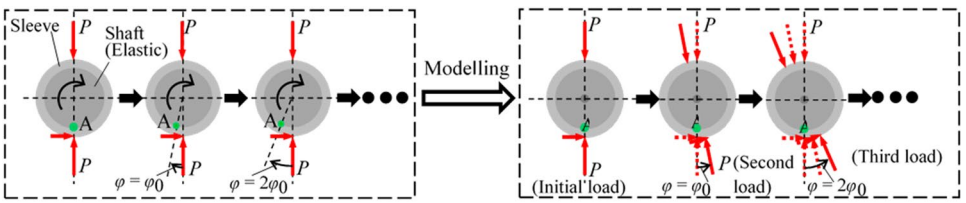

(a) Rotation of the real roll. (b) Rotation of the loads in the FEM model.

Fig. 10 The roll rotation can be replaced by discrete load shifting by the angle φ_0 on the fixed roll

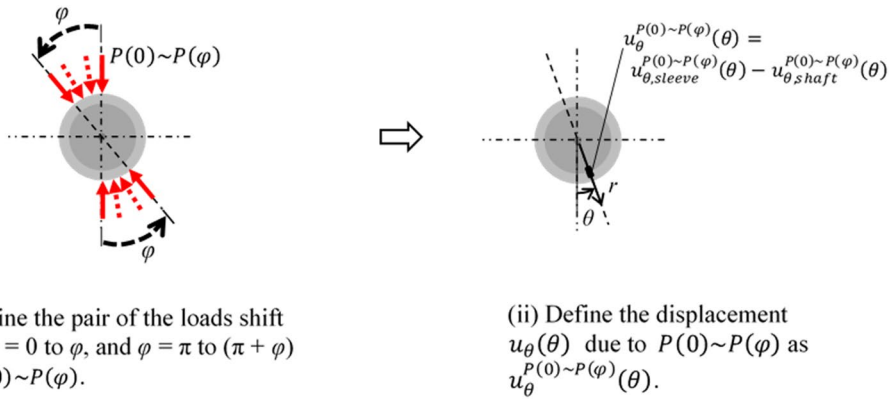

Fig. 11 Definition of interfacial displacement $u_\theta^{P(0)\sim P(\varphi)}(\theta)$ due to the load shifting $P(0) \sim P(\varphi)$

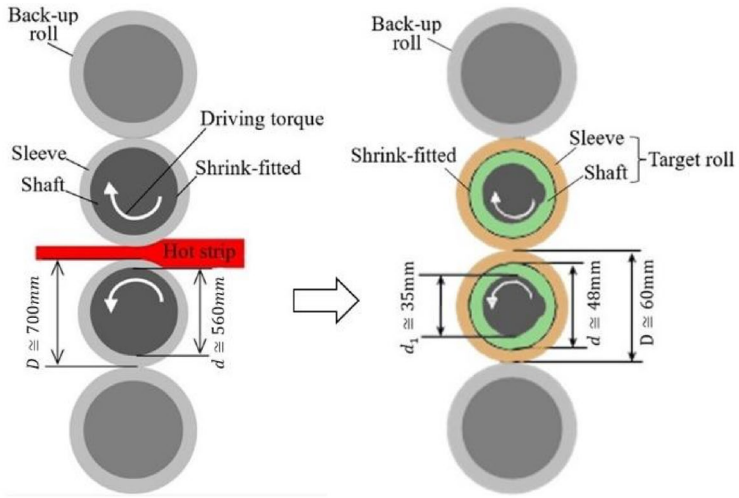

Fig. 12 Schematic illustration for (a) Real roll and (b) Miniature roll

$(x/a)^2 + (y/b)^2 + (z/c)^2 = 1, a = 1000\mu m, b = 250\mu m, c = 4000\mu m$ the stress concentration can be $K_t = 1.14$ [48]. In this study, the fatigue strength reduction is evaluated by using the parameter $\sqrt{\text{area}}$, which is the square root of the projected area of the defect onto a plane perpendicular to the maximum principal stress [49]. Then, the miniature roll's defect can be characterized by $\sqrt{\text{area}} = \sqrt{(\pi ab)/2} = 627\mu m$ from the defect geometry $a = 1000\mu\text{m}, b = 250\mu\text{m}$ in Fig. 14.

On the other hand, the defect depth $b' = 1$ mm was reported after slip in the hot rough rolling sleeve roll whose body diameter $D = 1150$ mm although the detail geometry is unknown [5, 6]. As shown in Fig. 3A, in this study, the real roll diameter $D = 700$ mm is considered, and the depth of the defect can be a bit smaller than $b' = 1$ mm although it can be larger than the defect depth $b = 0.25$mm of the miniature roll. Assume that the similar shape of the defect in Fig. 13 and Fig. 14 is formed due to the sllipage

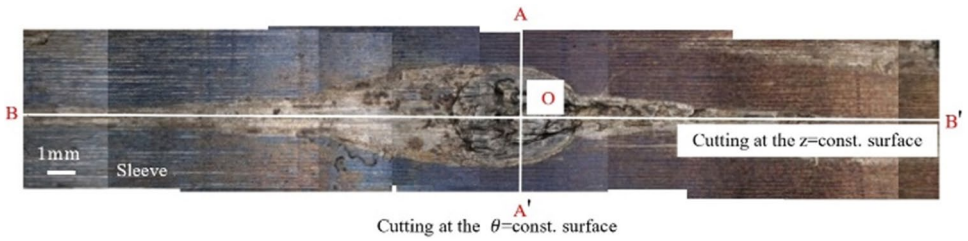

Fig. 13 Example of defect formed by the slippage on the sleeve surface to identify defect dimension observed in the miniature roll in Fig. 12 when the shrink-fitting ratio $\delta/d = 0.21 \times 10^{-3}$

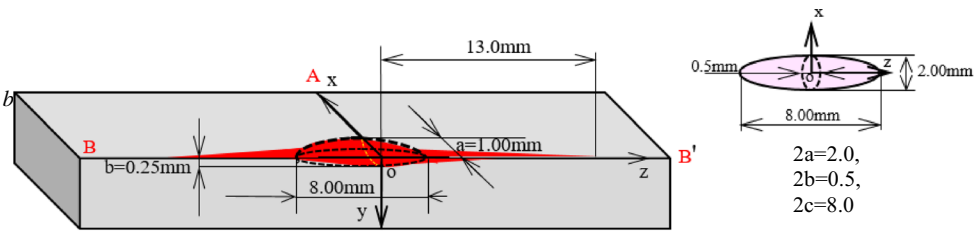

Fig. 14 Ellipsoidal plow defect geometry in Fig. 12 approximated by the equation $(x/a)^2 + (y/b)^2 + (z/c)^2 = 1,\ a = 1,\ b$ with the stress concentration factor $K_t = 1.14$

in the real roll. By assuming double sizes of the defect of the miniature roll, $\sqrt{\text{area}}$ dimension in the real roll can be $\sqrt{\text{area}} = \sqrt{\pi(2a)(2b)/2}$=$627 \times 2 = 1254\ \mu m$. Here $a = 1000\ \mu m$ and $b = 250\ \mu m$ is the defect dimension of the miniature roll.

Table 2 shows the specifications of the test work roll. The diameter of the test roll is about 1/10 of the diameter of the real roll. Table 3 shows the experimental conditions. Roll A denotes the roll without the shrink-fitting ratio of $\delta/d = 0$ and roll B denotes the roll with the shrink-fitting ratio of $\delta/d = 0.21 \times 10^{-3}$. In the experiment, the work roll is cooled with water at room temperature to prevent the change in shrink-fitting rate due to the temperature rise caused by friction due to the load. When the steady rotation speed reached 106 rpm or 212 rpm, a load of 1 ton is applied to ensure that the temperature change of the roll surface is within 5°C or less during the experiment by a contact thermometer.

Table 2 Test work roll specifications used in the miniature roll experiment in Fig. 12(b)

Specifications	
Size D, d, d_1 (mm)	60, 48, 35
Material	SCM440 quenched and tempered
Tensile strength σ_B (N/mm^2)	980
Hardness HB	Sleeve: 280 ~ 300 Shaft:305 ~ 330

Table 3 Conditions of the miniature roll experiment in Fig. 12(b)

Test roll		
Shrink-fitting ratio δ/d	Roll A	0
	Roll B	0.21×10^{-3}
Driving condition		
Test roll		Free rolling
Pair roll		Driven by the torque 457 Nm
Load P (ton)		1.0
Rotating speed (rpm)		106 ~ 212
Roll cooling: front side (L/min), back side		Water 0.25, 2.0
Roll temperature (°C): $\delta/d = 0.21 \times 10^{-3}$, 0		16.0 ~ 21.0
Number of rotations, n		Rotations until sleeve slip

Appendix C: Fatigue strength analysis results of bimetallic solid roll by simulation of cyclic loading caused by roll rotation

Figure 15 shows a bimetallic solid roll whose fatigue strength was considered in the previous paper [50, 51]. In the solid bimetallic roll, it was reported that the failures happened as the debonding at HSS/DCI boundary due to the stress σ_r as well as the roll center facture [5, 52]. Therefore, the risk of fatigue failure was evaluated at those critical points focusing on the stress σ_r. Figure 16 illustrates the stress amplitude versus mean stress diagram (σ_a-σ_m diagram) focusing on the fatigue limit under large compressive alternative loading $\sigma_m \leq 0$[50]. In this evaluation, the repeated maximum and minimum stress σ_r was considered during the roll rotation as the driving force causing the internal fatigue failure. Figure 17 illustrates those three critical points denoted by $B_0^{270}\big|_{\text{Rolledsteel}}$, $B_{750}^{270}\big|_{\text{Backuproll}}$, and C_0^0.

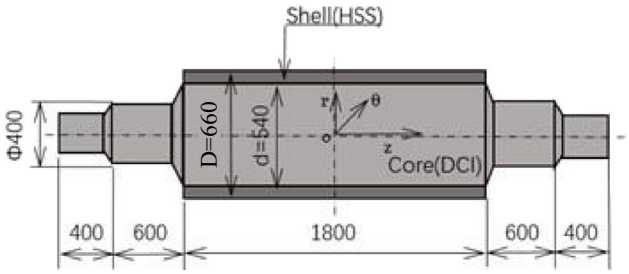

Fig. 15 Conventional bimetallic solid roll considered previously (mm)

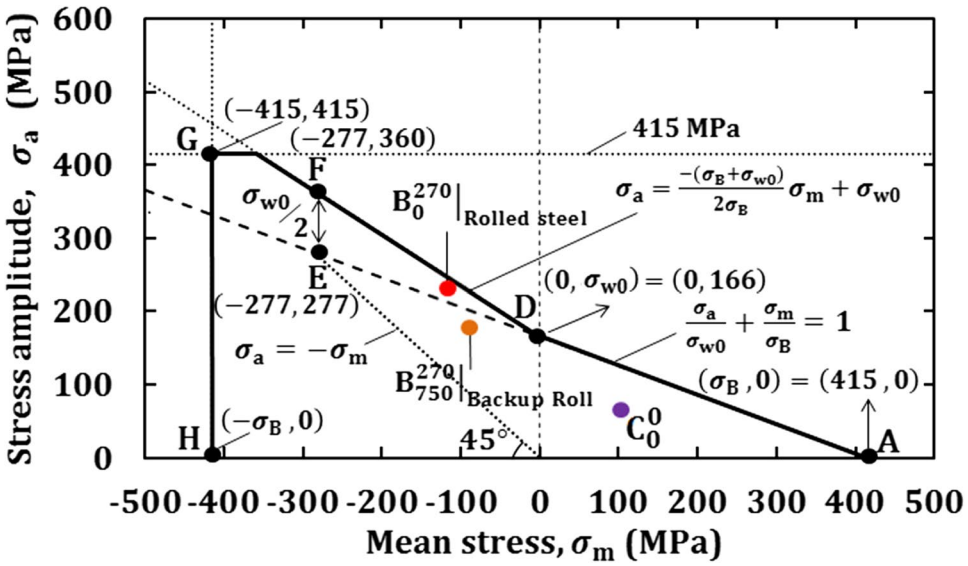

Fig. 16 Stress amplitude σ_a versus mean stress σ_m diagram to compare the fatigue failure risk at three critical points in the solid bimetallic roll in Fig. 15

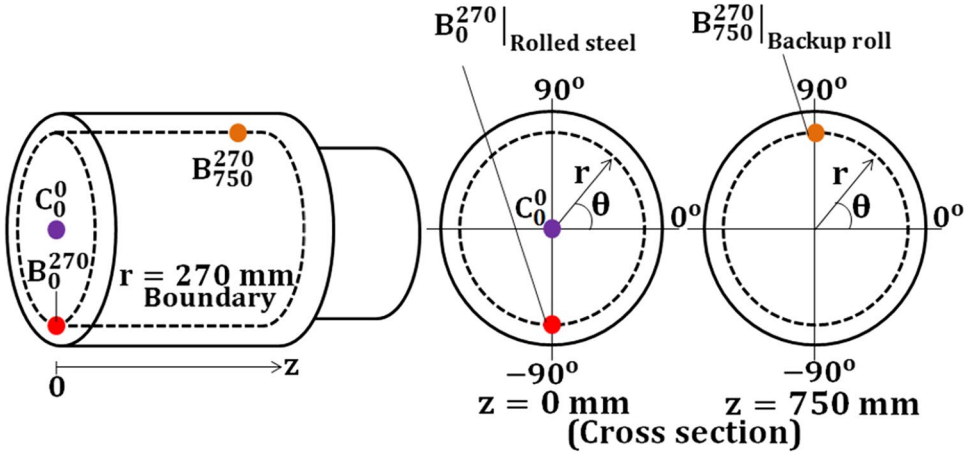

Fig. 17 Illustration of three critical points denoted by $B_0^{270}|_{Rolledsteel}$, $B_{750}^{270}|_{Backuproll}$, and C_0^0 where fatigue risk should be evaluated based on the analysis and experience

Author contribution R.A.R. and N-A.N. wrote the paper; N-A.N. supervised the research; Y.S. proposed and advised the research; R.A.R, X.Z., H.T., Y.T., and Y.T. performed the FEM simulation.

Declarations

Competing interests The authors declare no competing interests.

References

1. Shimoda H, Onodera S, Hori K (1966) Study on the residual deflection of large sleeved back-up rolls: 4th Report, Residual stresses of sleeved rolls. Trans Jpn Soc Mech Eng 32:689–694
2. Irie T, Takaki K, Tsutsunaga I, Sano Y (1979) Steel strip and section steel and thick rolling, processing. Tetsu-to-Hagane 65:293
3. Takigawa H, Hashimoto K, Konno G, Uchida S (2003) Development of forged high-speed-steel roll for shaped steel. CAMP-ISIJ 16:1150–1153
4. Sano Y (1993) Recent advances in rolling rolls. Proc of the No. 148–149 Nishiyama Memorial Technology Course, Tokyo, Japan, p 193–226
5. Sano Y (1999) Fatigue failure problem in the inside of roll body for hot strip rolling- Crack initiation problem and its estimation in the actual plant. The 245th JSMS Committee on Fatigue of Materials and the 36th JSMS Committee on Strength Design, Safety Evaluation, p 40
6. Matsunaga E, Tsuyuki T, Sano Y (1998) Optimum shrink fitting ratio of sleeve roll (Strength design of shrink fitted sleeve roll for hot strip mill-1). CAMP-ISIJ 11:362. https://ci.nii.ac.jp/naid/10002551803. Accessed 3 June 2020
7. Tutumi S, Hara S, Yoshi S (1971) The residual deflection of sleeved backup-up rolls. Tetsu-to-Hagane 57(5):818–22
8. Spuzic S, Strafford KN, Subramanian C, Savage G (1994) Wear of hot rolling mill rolls: an overview. Wear 176(2):261–271. https://doi.org/10.1016/0043-1648(94)90155-4
9. Noda NA, Hu K, Sano Y, Ono K, Hosokawa Y (2016) Residual stress simulation for hot strip bimetallic roll during quenching. Steel Res Int 87(11):1478–1488. https://doi.org/10.1002/srin.201500430

10. Noda NA, Sano Y, Takase Y, Shimoda Y, Zhang G (2017) Residual deflection mechanism for back-up roll consisting of shrink-fitted sleeve and arbor. J JSTP 58:66
11. Hu K, Xia Y, Zhu F, Noda NA (2017) Evaluation of thermal breakage in bimetallic work roll considering heat treated residual stress combined with thermal stress during hot rolling. Steel Res Int 89(4):1700368. https://doi.org/10.1002/srin.201700368
12. Goto K, Matsuda Y, Sakamoto K, Sugimoto Y (1992) Basic characteristics and microstructure of high-carbon high speed steel rolls for hot rolling mill. ISIJ Int 32:1184–1189
13. Ryu JH, Ryu HB (2003) Effect of thermal fatigue property of hot strip mill work roll materials on the rolled-in defects in the ultra-low carbon steel strips. ISIJ Int 43(7):1036–1039. https://doi.org/10.2355/isijinternational.43.1036
14. Park JW, Lee HC, Lee S (1999) Composition, microstructure, hardness, and wear properties of high-speed steel rolls. Metall Mater Trans A 30:399–409
15. Hattori T, Kamitani Y, Sugino K, Tomita H, Sano Y. Super cermet rolls for manufacturing ultra-fine-grained steel. International Conference on Tribology in Manufacturing Processes ICTMP 2007 International Conference 24–26 September 2007, Yokohama
16. Hamayoshi S, Ogawa E, Shimiz K, Noda NA, Kishi K, Koga S (2010) Development of large ceramic rolls for continuous hot-dip galvanized steel sheet production lines. Sokeizai 51(12):54–59
17. Noda NA, Sakai H, Sano Y, Takase Y, Shimoda Y (2018) Quasi-equilibrium stress zone with residual displacement causing permanent slippage in shrink-fitted sleeve rolls. Metals 8(12):998. https://doi.org/10.3390/met8120998
18. Sakai H, Noda NA, Sano Y, Zhang G, Takase Y (2019) Effect of driving torque on the interfacial creep for shrink-fitted bimetallic work roll. Tetsu-to-Hagane 105(12):1126–34. https://doi.org/10.2355/tetsutohagane.TETSU-2019-048
19. Noda NA, Rafar RA, Sakai H, Zheng X, Tsurumaru H, Sano Y, Takase Y (2021) Irreversible interfacial slip in shrink-fitted bimetallic work roll promoted by roll deformation. Eng Fail Anal 126:105465. https://doi.org/10.1016/j.engfailanal.2021.105465
20. Rafar RA, Noda NA, Tsurumaru H, Sano Y, Takase Y (2022) Novel design concept for shrink-fitted bimetallic sleeve roll in hot rolling mill. Int J Adv Manuf Technol 120:3167–3180. https://doi.org/10.1007/s00170-022-08954-2
21. Noda NA, Rafar RA, Sano Y (2021) Stress due to interfacial slip causing sleeve fracture in shrink-fitted work roll. Int J Mod Phys B 35(14n16):2140020. https://doi.org/10.1142/S0217979221400208
22. Noda NA, Sano Y, Aridi MR, Tsuboi K, Oda N (2018) Residual stress differences between uniform and non-uniform heating treatment of bimetallic roll: effect of creep behavior on residual stress. Metals 8(11):952
23. Soda N (1964) Bearing. Iwanami Shoten, Tokyo, p 196–203
24. Imai M (1959) Creep of the roller bearing. Lubrication: Journalof Japan Society of Lubrication Engineers 4(6):307–312
25. Murata J, Onizuka T (2005) Generation mechanism of inner ring creep. Koyo Eng J 166:41–47
26. Niwa T (2013) A creep mechanism of rolling bearings. NTN Tech Rev 81:100–103
27. Ten S (2006) Takemura, Yukawa. NSK Tech J 680:13
28. New Bearing Doctor: Diagnosis of bearing problems. Objective: Smooth & reliable operation. NSK, https://www.nsk.com/common/data/ctrgPdf/e7005c.pdf. 1997 [accessed 28 June 2020]
29. Zhan J, Takemura H, Yukawa K (2007) A study on bearing creep mechanism with FEM simulation. Proceedings of IMECE2007, Seattle, Washington, USA. https://doi.org/10.1115/IMECE2007-41366
30. Zhan J, Yukawa K, Takemura H (2009) Analysis of bearing outer ring creep with FEM. Advanced Tribology, Springer, Berlin, Heidelberg. https://doi.org/10.1007/978-3-642-03653-8_74
31. Noguchi S, Ichikawa K (2010) A study about creep between inner ring of ball bearing and shaft. Proceeding of Academic Lectures of the Japan Society for Precision Engineering, Japan. https://doi.org/10.11522/pscjspe.2010A.0.565.0
32. Teramoto T, Sato Y (2015) Prediction method of outer ring creep phenomenon of ball bearing under bearing load. Trans Soc Automot Eng Japan 46:355–360. https://doi.org/10.11351/jsaeronbun.46.355
33. Bovet C, Zamponi L (2016) An approach for predicting the internal behaviour of ball bearings under high moment load. Mech Mach Theory 101:1–22. https://doi.org/10.1016/j.mechmachtheory.2016.03.002
34. Maiwald A, Leidich E (2013) FE simulations of irreversible relative movements (creeping) in rolling bearing seats –influential parameters and remedies. World Congress on Engineering and Computer Science Vol II, San Francisco, USA. http://www.iaeng.org/publication/WCECS2013/WCECS2013_pp1030-1035.pdf. Accessed 4 June 2019
35. Schiemann T, Porsch S, Leidich E, Sauer B (2018) Intermediate layer as measure against rolling bearing creep. Wind Energy 21:426–440. https://doi.org/10.1002/we.2170
36. Miyazaki T, Noda NA, Ren F, Wang Z, Sano Y, Iida K (2017) Analysis of intensity of singular stress field for bonded cylinder and bonded pipe in comparison with bonded plate. Int J Adhes Adhes 77:118–137. https://doi.org/10.1016/j.ijadhadh.2017.03.019
37. Noda NA, Miyazaki T, Li R, Uchikoba T, Sano Y, Takase Y (2015) Debonding strength evaluation in terms of the intensity of singular stress at the interface corner with and without fictitious crack. Int J Adhes Adhes 61:46–64. https://doi.org/10.1016/j.ijadhadh.2015.04.005
38. Noda NA, Uchikoba T, Ueno M, Sano Y, Iida K, Wang Z, Wang G (2015) Convenient debonding strength evaluation for spray coating based on intensity of singular stress. ISIJ Int 55(12):2624–2630. https://doi.org/10.2355/isijinternational.ISIJINT-2015-458
39. Wang Z, Noda NA, Ueno M, Sano Y (2016) Optimum design of ceramic spray coating evaluated in terms of intensity of singular stress field. Steel Res Int 88:1–9. https://doi.org/10.1002/srin.201600353
40. Noda NA, Chen X, Sano Y, Wahab MA, Maruyama H, Fujisawa R, Takase Y (2016) Effect of pitch difference between the bolt-nut connections upon the anti-loosening performance and fatigue life. Mater Des 96:476–489. https://doi.org/10.1016/j.matdes.2016.01.128
41. Noda NA, Takaki R, Shen Y, Inoue A, Sano Y, Akagi D, Takase Y, Galvez P (2019) Strain rate concentration factor for flat notched specimen to predict impact strength for polymeric materials. Mech Mater 131:141–157. https://doi.org/10.1016/j.mechmat.2019.01.011
42. Matsuda S, Suryadi D, Noda NA, Sano Y, Takase Y, Harada S (2013) Structural design for ceramics rollers used in the heating furnace. Trans JSME Ser A 79(803):989–999
43. Noda NA, Suryadi D, Kumasaki S, Sano Y, Takase Y (2015) Failure analysis for coming out of shaft from shrink-fitted ceramics sleeve. Eng Fail Anal 57:219–235. https://doi.org/10.1016/j.engfailanal.2015.07.016
44. Noda NA, Xu Y, Suryadi D, Sano Y, Takase Y (2016) Coming out mechanism of steel shaft from ceramic sleeve. ISIJ Int 56(2):303–310. https://doi.org/10.2355/isijinternational.ISIJINT-2015-558
45. Zhang G, Sakai H, Noda NA, Sano Y, Oshiro S (2019) Generation mechanism of driving out force of the shaft from the shrink fitted ceramic roll by introducing newly designed stopper. ISIJ

Int 59(2):293–299. https://doi.org/10.2355/isijinternational.ISIJINT-2018-615
46. Marc Mentat team (2008) Theory and User Information, Vol. A, MSC, Software, Tokyo, p 713
47. Misumi-vona Top, Technical information, Dry coefficient of friction. https://jp.misumi-ec.com/tech-info/categories/plastic_mold_design/pl07/c0874.html. [accessed 2 March 2019]
48. Rafar RA, Noda NA, Taruya Y, Sano Y, Takase Y, Kondo K. Experimental verification of interfacial slip generation for shrink-fitted bimetallic work roll by using miniature roll, the 9th International Symposium on Applied Engineering and Sciences 2021 (SAES2021), 5th-8th December 2021
49. Murakami Y (2002) Metal fatigue: effects of small defects and nonmetallic inclusions. Elsevier Science, Oxford
50. Aridi MR, Noda NA, Sano Y, Takata K, Sun Z (2022) Fatigue failure analysis for bimetallic work roll in hot strip mills. Steel Res Int 93(2):2100313. https://doi.org/10.1002/srin.202100313
51. Aridi MR, Noda NA, Sano Y, Takata K, Sun Z, Takase Y (2022) Fatigue failure risk evaluation of bimetallic rolls in four-high hot rolling mills. Fatigue Fract Eng Mater Struct 45(4):1065–1087. https://doi.org/10.1111/ffe.13651
52. Sano Y, Kimura K (1987) Statistical analysis about crack and spalling on work roll for hot strip mill finishing rear stands. Tetsu-to-Hagane 73:78–85. https://doi.org/10.1111/ffe.13651
53. Ikeda T, Noda NA, Sano Y (2019) Conditions for notch strength to be higher than static tensile strength in high-strength ductile cast iron. Eng Fract Mech 206:75–88
54. Li XT, Wang MT, Du FS, Zhang GL (2014) Numerical simulation and model of control-efficiency of thermal crown of work rolls in cold rolling. J Cent South Univ 21:2160–2167. https://doi.org/10.1007/s11771-014-2166-2
55. Belzunce FJ, Ziadi A, Rodriguez C (2004) Structural integrity of hot strip mill rolling rolls. Eng Fail Anal 11:789–797. https://doi.org/10.1016/j.engfailanal.2003.10.004
56. Sekimoto Y, Tanaka K, Nakajima K, Kawanami T (1975) Effects of rolling condition on the surface temperature of work roll in hot strip mill. Tetsu-to-Hagane 61(10):2337–2349
57. Sekimoto Y (1982) Material and lifespan of hot rolling rolls. J Jpn Soc Technol Plasticity 23:952–957
58. Li CS, Yu HL, Deng GY, Liu XH, Wang GD (2007) Numerical simulation of temparatute field and thermal stress field of work roll during hot strip rolling. Iron Steel Res Int 14(5):18–21
59. Noda NA, Rafar RA, Taruya Y, Zheng X, Tsurumaru Y, Sano Y, Takase Y, Yakagawa K, Kondo K (2022) Interfacial slip verification and slip defect identification in shrink-fitted bimetallic sleeve roll used in hot rolling mill. Tribol Int. https://doi.org/10.1016/j.triboint.2022.107793